`

Deep learning-based aberration compensation improves contrast and resolution in fluorescence microscopy

Min Guo[1,2,*], Yicong Wu[2,3,^], Yijun Su[2,3,%], Shuhao Qian[1], Eric Krueger[2,%], Ryan Christensen[2,%], Grant Kroeschell[2,%], Johnny Bui[2,%], Matthew Chaw[2,%], Lixia Zhang[3], Jiamin Liu[3], Xuekai Hou[1], Xiaofei Han[2], Xuefei Ma[4], Alexander Zhovmer[4], Christian Combs[5], Mark Moyle[6], Eviatar Yemini[7], Huafeng Liu[1], Zhiyi Liu[1], Patrick La Riviere[8,9], Daniel Colón-Ramos[9,10], Hari Shroff[2,3,9,%]

1. Current address: State Key Laboratory of Modern Optical Instrumentation, College of Optical Science and Engineering, Zhejiang University, Hangzhou, China
2. Laboratory of High Resolution Optical Imaging, National Institute of Biomedical Imaging and Bioengineering, National Institutes of Health, Bethesda, Maryland, USA
3. Advanced Imaging and Microscopy Resource, National Institutes of Health, Bethesda, Maryland, USA
4. Center for Biologics Evaluation and Research, U.S. Food and Drug Administration, Silver Spring, MD, USA
5. NHLBI Light Microscopy Facility, National Institutes of Health, Bethesda, MD, USA
6. Department of Biology, Brigham Young University-Idaho, Rexburg, ID, USA
7. Department of Neurobiology, UMass Chan Medical School, Worcester, MA
8. Department of Radiology, University of Chicago, Chicago, IL, USA
9. MBL Fellows Program, Marine Biological Laboratory, Woods Hole, MA, USA
10. Wu Tsai Institute, Department of Neuroscience and Department of Cell Biology, Yale University School of Medicine, New Haven, CT, USA

^ Current address: Nanodelivery Systems and Devices Branch, Cancer Imaging Program, Division of Cancer Treatment and Diagnosis, National Cancer Institute, National Institutes of Health, Rockville, MD, USA

% Current address: Janelia Research Campus, Howard Hughes Medical Institute (HHMI), Ashburn, VA, USA

* Correspondence to guom@zju.edu.cn

Abstract

Optical aberrations hinder fluorescence microscopy of thick samples, reducing image signal, contrast, and resolution. Here we introduce a deep learning-based strategy for aberration compensation, improving image quality without slowing image acquisition, applying additional dose, or introducing more optics into the imaging path. Our method (i) introduces synthetic aberrations to images acquired on the shallow side of image stacks, making them resemble those acquired deeper into the volume and (ii) trains neural networks to reverse the effect of these aberrations. We use simulations to show that applying the trained 'de-aberration' networks outperforms alternative methods, and subsequently apply the networks to diverse datasets captured with confocal, light-sheet, multi-photon, and super-resolution microscopy. In all cases, the improved quality of the restored data facilitates qualitative image inspection and improves downstream image quantitation, including orientational analysis of blood vessels in mouse tissue and improved membrane and nuclear segmentation in *C. elegans* embryos.

`

Introduction

Fluorescence microscopes offer diffraction-limited imaging only when optical aberrations are absent. Such aberrations can arise due to optical path length differences introduced anywhere in the imaging path, including from instrument misalignment, optical imperfections, or differences in refractive index between the heterogenous and refractile sample, immersion media, or objective immersion oil. Sample-induced optical aberrations usually dominate and are often the reason that three-dimensional (3D) fluorescence image volumes show obvious deterioration in image signal-to-noise ratio (SNR), contrast, and resolution deeper into the image volume.

One method of compensating for these aberrations is via adaptive optics (AO[1,2]), a broad class of techniques that measure the aberrated wavefront and subsequently apply an equal and opposite 'corrective' wavefront, restoring diffraction-limited[3] or even super-resolution[4] imaging throughout the image volume. Once the aberrated wavefront is determined, an adaptive element such as a deformable mirror or spatial light modulator is used to apply the correction. Although these methods are effective, the process of determining the wavefront typically slows acquisition and/or applies more illumination dose than imaging without AO. From a practical perspective, implementing AO is nontrivial and adds considerable expense to the underlying microscope. Thus, AO remains the province of relatively few labs, and there is a need for new methods that can reverse the effects of optical aberrations without sacrificing temporal resolution, imparting more dose to the sample, or adding additional hardware to the microscope.

Deep learning approaches can computationally reverse image degradation, and have been used successfully in denoising[5,6], deconvolution[7,8], and super-resolution applications[9,10]. By incorporating information about the underlying object, such methods can also learn to predict the wavefront associated with aberrated images[11-13]. With sufficient training data (matched pairs of diffraction-limited and aberrated data), we reasoned that a neural network ought to be able to directly predict the diffraction-limited image from the aberrated image. The challenge then becomes accumulating appropriate training data, which would ideally be obtained without relying on AO.

Here we address this problem by (i) introducing synthetic aberrations to easily obtained near-diffraction limited data so that they resemble aberrated data and (ii) training neural networks to reverse the effect of these aberrations. We use simulations to show that application of our 'content-aware' approach outperforms other image restoration methods, including deconvolution with the known aberrated point spread function (PSF). We then apply our techniques to diverse volumetric data captured with confocal, light-sheet, multi-photon, and super-resolution microscopes, finding that in all cases, resolution and contrast are substantially improved over the raw data. In addition to facilitating biological inspection, the restored data also enhanced quantitative investigation, including orientational analysis of blood vessels in mouse tissue and improved accuracy of membrane and nuclear segmentation in *C. elegans* embryos.

Results

Compensating for aberrations with deep learning

First, we intentionally synthetically aberrate the images acquired by fluorescence microscopes given knowledge of the physics of image formation[14,15] (**Fig. 1, Methods, Supplementary Note 1**). Aberrations are chosen so that the aberrated images resemble those acquired deeper into the sample,

`

where aberrations are more pronounced. The key insight of our approach is that the 'shallow' images on the 'near side' of the three-dimensional fluorescence volume are usually near-diffraction-limited and thus provide ground truth data that can be used to train a network to reverse the effect of the synthetically introduced aberrations. The trained neural network model (termed 'DeAbe') can then be used to reverse depth-dependent blurring on data unseen by the network, effectively mitigating the effect of aberrations without recourse to AO.

To benchmark our method, we began by simulating 3D phantoms consisting of randomly oriented and positioned dots, lines, spheres, circles, and spherical shells. We then degraded these structures by adding random aberrations and noise and evaluated the extent to which DeAbe could reverse the degradation (**Fig. 1b, Supplementary Figs. 1-5**). Visual assessments in lateral (**Fig. 1c, d, Supplementary Video 1**) and axial (**Fig. 1e, Supplementary Video 2**) views, as well as quantitative comparisons (**Fig. 1f**) demonstrated that the DeAbe model outperformed blind deconvolution[16], Richardson-Lucy deconvolution with an ideal point spread function (PSF), and even Richardson-Lucy deconvolution with the aberrated PSF (known in these simulations, but unknown in general). We attribute the superior performance of DeAbe to its ability to learn a sample-specific prior, thereby better conditioning its solution relative to Richardson-Lucy deconvolution.

Importantly, simulations allowed us to further characterize DeAbe, offering insight into the regimes in which the method excels and where performance suffers. First, we found optimal performance when aberration magnitudes in the training data match the aberration magnitude in the test data (**Supplementary Fig. 1**). Over the conditions we tested, the model improved images contaminated with root mean square (RMS) wavefront distortion exceeding four radians (the highest value we tested), although performance degrades as wavefront distortion increases. Second, although we performed tests with training data containing up to the 7th Zernike order, the improvement offered past order four (the value used in this work) is negligible (**Supplementary Fig. 2**). Third, DeAbe trained on a mixture of Zernike basis functions also provides notable improvement on images corrupted solely by individual Zernike functions (**Supplementary Fig. 3**), although dedicated models trained to correct specific Zernike modes are better if these modes are known in advance (**Supplementary Fig. 4**). Finally, although DeAbe's performance suffers in the presence of noise, it still offers noticeable visual and quantitative improvements in image quality for SNR above ~5 (**Supplementary Fig. 5**).

Computational aberration compensation improves image quality on diverse volumetric data

We subsequently applied DeAbe to experimental data acquired with different microscope modalities, in each case training models on images derived from the shallow side of image volumes (**Fig. 2, Supplementary Fig. 6, Supplementary Table 1**). First, we imaged live *C. elegans* embryos expressing a pan-nuclear GFP-histone marker with inverted selective plane illumination microscopy (iSPIM)[17,18], finding that the raw image data displayed progressive loss of contrast and resolution as a function of increasing depth, making it difficult or impossible to discern subnuclear structure (or even individual nuclei) at deeper imaging planes (**Fig. 2a, i, Supplementary Video 3**). By contrast, the DeAbe prediction restored these structures, also improving axial views (**Fig. 2a, iii**). Richardson-Lucy deconvolution also offered some improvement in image quality, albeit not to the extent of the DeAbe prediction, while also undesirably amplifying noise (**Fig. 2a, ii**). Second, we used spinning-disk confocal microscopy to image thicker adult *C. elegans* expressing the multicolor NeuroPAL transgene[19], used for resolving neuronal identities. Depth-dependent image degradation produced raw images with dim or diffuse nuclear signal

`

in each color channel. The DeAbe prediction improved SNR dramatically (**Supplementary Fig. 7, Supplementary Video 4**), which we suspect may prove useful in improving the accuracy of neuronal identification. Third, we applied DeAbe to images of NK-92 cells stained with Alexa Fluor 555 wheat germ agglutinin and embedded in collagen matrices, acquired with instant SIM[20], a super-resolution imaging technique (**Fig. 2b-d**, **Supplementary Fig. 8, Supplementary Video 5**). Post deconvolution, the DeAbe prediction better resolved clusters of membrane-bound glycoproteins, intracellular vesicles, and membranes ('DeAbe+', **Fig. 2c, d**) than the raw (or deconvolved raw, **Supplementary Fig. 8**) data, especially near the limits of the 45 μm thick imaging volume. Fourth, we used two-photon microscopy to image live murine cardiac tissue expressing Tomm20-GFP, marking the outer mitochondrial membrane (**Fig. 2e**). Although mitochondrial boundaries were evident in the raw data 20 μm into the volume, aberrations caused a progressive loss in resolution that hindered visualization of subcellular structure at greater depths (**Fig. 2e, f**). The DeAbe prediction restored resolution throughout the 150 μm thick volume (**Fig. 2f, Supplementary Fig. 9, Supplementary Video 6**), unlike Richardson-Lucy deconvolution (**Fig. 2f**) which amplified noise without restoring the mitochondria. The DeAbe prediction similarly improved contrast and resolution when applied to volumes of fixed mouse liver stained with membrane labeled tdTomato, imaged with two-photon microscopy (**Supplementary Video 7)**.

Next, we applied DeAbe to samples ~10,000-fold larger in volumetric extent (**Fig. 3a, Supplementary Video 8**). We fixed and CLARITY[21]-cleared E11.5 mouse embryos immunostained for neurons (Alexa Fluor TuJ1) and blood vessels (Alexa Fluor 594) and imaged them with low magnification confocal microscopy. Although tissue clearing nominally produces a sample with the same refractive index everywhere, we still observed pronounced depth-dependent degradation from the 'near' to 'far' side of the embryo, including in intensity (likely due to photobleaching during the acquisition) and resolution. We were able to largely reverse this deterioration by digitally compensating for photobleaching[22] (**Methods**), applying DeAbe, and finally deconvolving the data (**Fig. 3b, Supplementary Fig. 10**). While the improvement in image quality was particularly striking in axial views (**Fig. 3b**), restorations also improved the appearance of fibrillar structures in lateral views, in both channels, throughout the volume (e.g., the vicinity of the vagus nerve and its associated nerve roots, **Fig. 3c, d**).

We further investigated this qualitative impression by using automated tools[23,24] to quantitatively assess the mean 3D orientation and directional variance (a measure of the spread in angular orientation) at each voxel in the blood vessel channel (**Fig. 3e-g**, **Supplementary Figs. 11, 12, Supplementary Video 9**). The DeAbe restoration resulted in cleaner separation between vessels, which aided voxel-wise quantification of these metrics even in dense regions containing many crisscrossing vessels (**Fig. 3e, Supplementary Video 9**). In deeper regions of the volume (**Fig. 3f**), the DeAbe results produced narrower angular histogram distributions of vessels than the noisy raw data (**Fig. 3f**). The improvement in quantification was also reflected in directional variance analysis. For example, when visually inspecting different regions of interest (ROI) with differential vessel alignment (**Fig. 3g**, comparing vicinity of aortic arches, (ROI 1), to diencephalon, (ROI 2)) we observed a greater difference in mean directional variance when using the DeAbe reconstruction vs. the raw data (**Supplementary Fig. 12**).

Incorporating DeAbe in multi-step restoration further enhances resolution and contrast in 4D imaging applications

`

Given the performance of DeAbe thus far, we wondered if we could further boost image quality by combining DeAbe with additional networks designed to enhance spatial resolution. To test this possibility, we acquired dual-view light sheet microscopy (diSPIM[25,26]) volumetric time-lapse ('4D') recordings of *C. elegans* embryos expressing labels marking cell membranes and nuclei, and then passed the raw single-view data through three networks designed to sequentially compensate for aberrations (i.e., DeAbe), deconvolve the resulting predictions ('DL Decon'), and improve resolution isotropy[5] ('DL Iso', **Fig. 4a-d, Supplementary Figs. 13-16**). As expected, (**Fig. 4a**), the raw data showed increasing depth-dependent degradation in resolution and contrast, which confounded our ability to discern distinct nuclei or cell boundaries on the 'far' side of the volume. In comparison, the multi-step procedure offered striking improvements in resolution and contrast in both nuclear and membrane channels, largely alleviating the degradation (**Fig. 4a, b, Supplementary Figs. 14, 15, Supplementary Video 10**). Ablation experiments in which one or more of the networks were removed produced inferior results, further substantiating our hypothesis that the gains in image quality benefited from applying all three networks (**Supplementary Fig. 17**). In the membrane channel, the multi-step restoration enabled us to automatically segment cell boundaries more accurately than in the raw data and further refine the segmentations manually up to 421 cells (**Fig. 4c, Supplementary Fig. 16, Supplementary Video 11**), exceeding previous efforts limited to the 350-cell stage[27]. The automatic segmentation additionally provided a cell count closer to manual ground truth[28] than either the raw data or a subset of the networks (**Fig. 4d**).

Next, we explored replacing the final network (DL Iso) with a network designed to further enhance resolution based on ground truth acquired with expansion microscopy[9,29] ('DL Expan', **Supplementary Fig. 13b**). After verifying that DL Expan improved resolution more than 2-fold on data unseen by the model (**Supplementary Fig. 18**), we applied the new multi-step restoration method to *C. elegans* embryos expressing a GFP-membrane marker labeling head neurons and gut cells (**Fig. 4e**). Compared to the raw data, the enhanced resolution offered by the deep learning prediction better resolved closely spaced membranes within and between cells (**Fig 4f-h, Supplementary Figs. 19, 20**). This capability proved especially useful when tracking the development of neurites projecting in the nerve ring, a neuropil that constitutes the brain of the animal, and which is composed of hundreds of tightly packed interwoven neurites. While the position of the neurites within the neuropil determines circuit identity and connectivity, the sequence of events leading to its innervation has not been described because of limits in resolving these structures. We focused our analyses on the closely positioned neurons AIY and SMDD, which we identified based on morphology by comparison to labeled images in ref.[30] and ref.[31]. SMDD is a central pioneering neuron in the nematode brain[31-33], while its sister cell AIY[30] is a first layer interneuron[34] involved in thermotaxis and locomotion[35]. Observing both neurons over our 120-minute recording, we found that SMDD's neurites grew out first, followed by AIY's neurite. AIY's neurite entered the nerve ring after SMDD, consistent with the SMDD's role as a pioneer neuron (**Fig 4i, Supplementary Video 12**). Such developmental dynamics were difficult or impossible to observe in the raw data (**Supplementary Fig. 21**), or joint deconvolutions of the dual-view data due to artifacts resulting from motion between the two views (**Supplementary Fig. 22**). Finally, to illustrate that these gains in image quality can be extended to a different label imaged in a different microscope, we also restored images of nuclei labeled with a GFP histone marker and acquired with high NA diSPIM[18], finding similarly dramatic improvements in contrast and resolution (**Supplementary Fig. 23, Supplementary Videos 13, 14)**.

`

Discussion

As we show on diverse microscopes and samples, DeAbe can compensate for optical aberrations without recourse to AO, improving SNR, contrast, and resolution in fluorescence microscopy volumes. We suspect this capability will be useful for most labs, which lack access to sophisticated AO setups but still wish to improve the quality of imaging volumes acquired using existing hardware. Besides improving the qualitative appearance of images (**Fig. 1-4**), which facilitates inspection of biological features deep within imaging volumes, DeAbe also quantitatively improves downstream image analysis. We highlight this capability by refining vessel segmentation in large, cleared tissue samples (**Fig. 3e-g**) and in enhancing the segmentation of densely packed nuclei and membranes in *C. elegans* embryos (**Fig. 4**). The latter capability may prove particularly useful in the creation or extension of 4D morphological atlases[27], which depend on high quality image data.

Several caveats are worth noting in the context of current limitations and with an eye towards future applications. First, the performance of DeAbe depends critically on the quality of the training data, and specifically on the assumption that fluorescently labeled structures are similar throughout the image volume. While this assumption was met for the samples in this work, we encourage caution when applying DeAbe on highly heterogenous specimens. Second, although here we mainly trained on semi-synthetic data (**Fig. 2-4**), it would also be worth investigating how well the training derived from fully synthetic data[7] (**Fig. 1**) generalizes to experimental data. Such an approach might prove useful in ameliorating system aberrations introduced by microscope hardware. Third, we focused here on correcting depth-dependent aberrations, in which the training data was corrupted by a constant aberration in each image plane. A useful future direction would be to extend our approach to explicitly account for laterally varying aberrations, as such aberrations are problematic particularly for large specimens. Finally, although we used a mixture of random low-order aberrations to train our model, enhanced performance is likely if aberrations specific to the sample (or instrument) can be inferred and used in the training procedure (**Supplementary Fig. 4**).

Author Contributions

Conceived project and directed research: H.S. Implemented DeAbe framework: M.G. Designed simulations: M.G., Y.W., H.S. Wrote software: M.G., Y.W., J.L., X.Han, S.Q., Z.L. Designed experiments: M.G., Y.S., R.C., X.M, A.Z., C.C., M.M., E.Y., D.C-R., H.S. Prepared samples: M.G., Y.S., E.K., R.C., G.K., J.B., M.C., L.Z., X.M., A.Z., C.C., M.M., E.Y. Performed experiments: M.G., Y.S., E.K., R.C., G.K., J.B., M.C., X.Han, X.M., A.Z., C.C., M.M., E.Y. Designed and performed segmentation analysis: M.G., Y.S., J.L., X. Hou, S.Q., Z.L. All authors examined and analyzed data. Wrote manuscript: M.G. and H.S., with advice from all authors. Provided biological insight and advice: R.C., X.M., A.Z., C.C., M.M., E.Y., D.C-R. Supervised research: E.Y., H.L, Z.L., P.L-R., D.C-R., H.S.

Acknowledgments

We thank O.H. for supporting the NeuroPAL work in his lab and allowing us to use the data generated therein for this paper, Robert Weigert (NCI) for the gift of the fixed mouse liver sample, Nikolaj Reiser for helpful discussions, and Courtney Johnson and Xuesong Li for their comments on the manuscript. This research was supported by the intramural research programs of the National Institute of Biomedical Imaging and Bioengineering and the National Heart, Lung, and Blood Institute within the National

`

Institutes of Health (NIH). This work was supported by the Howard Hughes Medical Institute (HHMI). This article is subject to HHMI's Open Access to Publications policy. HHMI laboratory heads have previously granted a non-exclusive CC BY 4.0 license to the public and a sub-licensable license to HHMI in their research articles. Pursuant to those licenses, the author-accepted manuscript of this article can be made freely available under a CC BY 4.0 license immediately upon publication. This research is funded in part by the Gordon and Betty Moore Foundation. We thank the Office of Data Science Strategy, NIH, for providing a seed grant enabling us to test and validate the initial deep learning frameworks using cloud-based computational resources. H.S., P.L.R. and D.C.-R. acknowledge the Whitman and Fellows program at MBL for providing funding and space for discussions valuable to this work. Z.L. acknowledges the funding support from Natural Science Foundation of Zhejiang Province (LR20F050001). H.L. acknowledges the funding support from the National Key Research and Development Program of China (2020AAA0109502), the National Natural Science Foundation of China (U1809204) and the Talent Program of Zhejiang Province (2021R51004). E.Y. acknowledges support from the Esther A. and Joseph Klingenstein Fund, the Simons Foundation, and the Hypothesis Fund. X.M. and A.Z. were supported by Intramural FDA funding.

Methods

Deep learning-based de-aberration model

Building a de-aberration model (DeAbe) requires appropriate training data and the use of a neural network. First, based on the physics of image formation, we derived forward imaging models that allowed us to synthetically aberrate the data produced for multiple systems, including wide field, light sheet, confocal, two photon, and super-resolution structured illumination microscopes (**Supplementary Note 1**). Second, we extracted subvolumes from the shallow side of the experimentally acquired image stacks, using these data as ground truth. Third, based on the forward imaging models, we synthetically added aberrations to the ground truth images so that they resembled aberrated data present deeper within the image stacks. Together, the paired ground truth data and associated synthetically degraded data constitute training pairs. Fourth, we used these training pairs in conjunction with our 3D RCAN network[9] to train a DeAbe model to reverse the effect of synthetic aberration. Finally, we applied the trained network to reduce the effects of aberrations in experimentally acquired image volumes unseen by the network.

We define the 'shallow side' of an image stack by the planes nearest to the detection objective, which are typically contaminated with least aberration and thus offer the best image quality. We then selected subvolumes on the shallow side ('shallow subvolumes') by visually inspecting image quality in real and Fourier space (**Supplementary Fig. 6, Supplementary Table 1**). We extracted shallow subvolumes from image stacks by manually cropping with ImageJ when image size and content differed substantially across a given specimen type, or automatically with customized ImageJ macros when considering specimens with more stereotyped image size and content (e.g., as for time-lapse image volumes). For the cleared mouse embryo images (**Fig. 3**), the shallow subvolumes were further divided into smaller subvolumes (~80 MB/volume) due to their large volume size in raw data (**Supplementary Table 1**).

`

As described in **Supplementary Note 1**, we expressed the aberrated wavefront $\phi(r,\theta)$ at the back focal plane of the objective using Zernike basis functions $\phi_m(r,\theta)$ and associated Zernike coefficients c_m

$$\phi(r,\theta) = \sum_{m=0}^{M} c_m \phi_m(r,\theta), \quad (1)$$

with M the maximum Zernike index chosen in our aberration.

We generated synthetic aberrations by using semi-randomly generated Zernike coefficients (**Fig. 1a**). We used the ANSI convention[36] when indexing the Zernike coefficients, customizing aberrations by using different Zernike coefficients for different datasets acquired from different microscopes. For all experimental datasets, we added aberrations up to the 4th Zernike order (i.e., *M* = 14), except for piston and tilt components (Z = 0, 1, 2). The amplitudes of the Zernike coefficients were randomly generated, but subject to pre-defined bounds. We initially set an upper bound of 0.5 rad for all Zernike coefficients, then added an additional 1 rad for defocus (Z = 4) and spherical (Z = 12) components to mimic the more severe contamination caused by defocus and spherical aberrations commonly encountered in experimental datasets, i.e:

$$\begin{cases} c_z = 0, & for\ Z = 0,1,2 \\ |c_z| \le 1.5, & for\ Z = 4,12 \\ |c_z| \le 0.5, & otherwise\ for\ Z \le M, \end{cases} \quad (2)$$

with M = 14 for all experimental datasets.

For each shallow side subvolume, 10 independent sets of aberrations were generated and used for synthetic degradation, thereby augmenting the data 10-fold. Processing was performed with custom MATLAB code (MathWorks, R2022b), with further details provided in the *Code availability* section.

We employed 3D RCAN (https://github.com/AiviaCommunity/3D-RCAN), appropriate for 3D image volumes, for generating the DeAbe model based on the training data pairs. We trained individual DeAbe models for each microscope and each sample type. For training, we set the number of epochs to 200; the number of steps per epoch to 400; the training patch size to 64 × 64 × 64; the number of residual blocks to 5; the number of residual groups to 5; and the number of channels to 32. The training was performed within Python 3.7.0 on a Windows 10 workstation (CPU: Intel Xeon, Platinum 8369B, two processors; RAM: 256 GB; GPU: NVIDIA GeForce RTX 3090 with 24 GB memory). More details on datasets and training parameters are listed in **Supplementary Table 1**.

Multi-step image restoration with deep learning

The multi-step image restoration pipeline combines the DeAbe model with two additional networks to progressively improve image resolution and contrast: (1) the DeAbe model to reverse degradation from aberrations ("DL DeAbe"); (2) a deconvolution network designed to mimic the image quality improvement afforded by multiview imaging ("DL Decon", see the section *Deep learning-based deconvolution*); (3) an axial resolution enhancement network to improve resolution isotropy ("DL Iso", see the section *Deep learning-based axial resolution enhancement*); or a network designed to predict the improved resolution provided by expanded samples ("DL Expan", see the section *Deep learning-based expansion*).

Deep learning-based deconvolution

`

As for our previous attempts at deep-learning based multiview deconvolution[8], we used a single-view image volume as input, and attempted to restore image resolution and contrast that approximated the result from multiview joint deconvolution. The training data were acquired by dual-view light sheet microscopy[25], either a 'symmetric' diSPIM equipped with 0.8/0.8 NA objectives[26] (**Fig 4e-i, Supplementary Figs. 17-22**) or a higher NA 'asymmetric' diSPIM equipped with 1.1 / 0.67 NA objectives[18] (**Fig 4a-d, Supplementary Figs. 14-16, 23**). First, raw images were de-aberrated with the DeAbe model. Then de-aberrated images from the two views were jointly deconvolved to achieve reconstructions with near isotropic spatial resolution and good image quality throughout the reconstruction. With training data consisting of the single-view de-aberrated images as input and the jointly deconvolved images as ground truth, we then used another 3D RCAN for the deconvolution model (DL Decon). For all datasets, the number of epochs for training was 200; the number of steps per epoch was 400; the training patch size was 64 × 64 × 64; the number of residual blocks was 5; the number of residual groups was 5; and the number of channels was 32. The training was performed within Python 3.7.0 on a Windows 10 workstation (CPU: Intel Xeon, Platinum 8168, two processors; RAM: 512 GB; GPU: Nvidia Quadro RTX6000 with 24 GB memory). We note that although training DL Decon required dual-view image volumes, applying DL Decon needs only single-view image volumes acquired from single-view light sheet microscopy (iSPIM).

Deep learning-based axial resolution enhancement

The images predicted by the DL Decon model were not perfectly isotropic, i.e., the axial resolution (although improved over the raw input images) is worse than the lateral resolution. Thus, for some experiments we used an additional network to enhance axial resolution (DL Iso, **Fig. 4a, b, Supplementary Figs. 14-17, Supplementary Videos 10, 11**). CARE[5] software (https://github.com/CSBDeep/CSBDeep) was employed to train the a 'DL Iso' model based on the predictions derived from serially applying the DeAbe and Decon models to raw input images. We used 100 3D volumes, each spanning 360 × 480 × 310 voxels, for training data. Training was performed on the xy planes (lateral views), using a 2D PSF (consisting of a point blurred with a 1D Gaussian function, sigma = 2.5 pixels along the y dimension) an axial downsampling factor of 6, and a patch size of 64 × 64 to create training pairs. The training was performed within Python 3.7.0 on a Windows 10 workstation (CPU: Intel Xeon, Platinum 8168, two processors; RAM: 512 GB; GPU: Nvidia Quadro RTX6000 with 24 GB memory).

Deep learning-based expansion

As an alternative to DL Iso, we also trained a model to improve the resolution based on data acquired with expansion microscopy (DL Expan). First, physically expanded samples (**Supplementary Fig. 18**) were imaged on the symmetric 0.8 NA diSPIM. Second, dual-view raw images were jointly deconvolved and used as ground truth images. Third, the ground truth images were synthetically degraded to resemble low-resolution conventional images acquired on the diSPIM, following our previous procedure[9]. Last, the 3D RCAN network was employed to train the DL Expan model based on the training data (i.e., synthetically degraded and ground truth pairs).

For the worm embryo data with DAPI labeled nuclei (**Supplementary Fig. 23**), dual-view raw image volumes from 15 expanded worm embryos were acquired and jointly deconvolved to produce 15 high-resolution image volumes. These 15 volumes were then synthetically degraded to generate low-resolution images. For the worm embryo data with TTX3B neurites labeled (**Fig 4e-i**, **Supplementary**

`

Figs. 18-21), dual view image volumes from 71 expanded worm embryos were acquired and manually cropped to select regions containing TTX3B neurites (this was necessary given the sparsely labeled neurites present in the raw images). Cropped images were jointly deconvolved to produce 71 high-resolution image volumes. These 71 volumes were then synthetically degraded to generate synthetic low-resolution image data. For each dataset, the low-resolution and high-resolution paired volumes were then used to train the 3D RCAN based DL Expan model. The number of epochs for training was set to 300; the number of steps per epoch to 400; the training patch size to 64 × 64 × 64; the number of residual blocks to 5; the number of residual groups to 5; and the number of channels to 32. The training was performed within Python 3.7.0 on a Windows 10 workstation (CPU: Intel Xeon, Platinum 8369B, two processors; RAM: 256 GB; GPU: NVIDIA GeForce RTX 3090 with 24 GB memory).

Simulations on phantom objects

To evaluate the quality and performance of our DeAbe model, we generated 3D phantom objects consisting of five types of structures in MATLAB (Mathworks, R2022b, with the Image Processing Toolbox): dots, lines, circles, spheres, and spherical shells[22]. Phantoms were randomly oriented and located in a volume of 256 × 256 × 256 voxels, with voxel size 0.13 × 0.13 × 0.13 μm^3. We simulated the blurring introduced by light sheet microscopy (**Supplementary Note 1**) by convolving the phantom with an ideal, noise-free PSF resembling that of our light sheet system (with 1.1 NA water dipping objective, detection wavelength of 0.532 μm and an illumination light sheet thickness of 2 μm). Aberrated data was generated by altering the ideal PSF according to the synthetic aberration procedure described above.

To create synthetic aberrations, we adopted Equation (1) and generated Zernike coefficients semi-randomly in MATLAB, with each Zernike coefficient c_m subject to a pre-defined upper bound T_m:

$$|c_m| \leq T_m, \quad for\ m \leq M, \tag{3}$$

with m the Zernike index following the ANSI convention and M the maximum Zernike index.
We omitted piston and tilt components (m = 0, 1, 2) and weighted lower order Zernike components (Defocus m =4, astigmatism m=3,5, and spherical m=12) more as these aberrations are commonly observed in real samples:

$$T_m = \begin{cases} 0, & for\ m = 0,1,2 \\ 1.5, & for\ m = 3,4,5,12 \\ 0.5, & otherwise\ for\ m \leq M, \end{cases} \tag{4}$$

with M defined based on the desired Zernike order:

$$M = \begin{cases} 9, & for\ Zernike\ order\ of\ 3 \\ 14, & for\ Zernike\ order\ of\ 4 \\ 20, & for\ Zernike\ order\ of\ 5 \\ 27, & for\ Zernike\ order\ of\ 6 \\ 35, & for\ Zernike\ order\ of\ 7 \end{cases}. \tag{5}$$

For **Supplementary Fig. 2**, we varied M to explore the effect of different Zernike orders on de-aberration performance by setting $M = 9, 14, 20, 27, \text{and } 35$ corresponding to Zernike orders 3-7. For all other simulations, we set $M = 14$.
The Root Mean Square (RMS) wavefront distortion of an aberration with Zernike coefficients c_m ($m = 3, 4, 5, \ldots, M$) is:

`

$$RMS_c = \sqrt{\sum_{m=3}^{M} {c_m}^2}. \quad (6)$$

The RMS wavefront distortion for aberrations defined by upper bounds T_m ($m = 3, 4, 5, \ldots, M$) is:

$$RMS_T = \sqrt{\sum_{m=3}^{M} {T_m}^2}. \quad (7)$$

To create training data, we synthetically aberrated phantoms with two types of aberrations:

1) a random mixture of aberrations containing different Zernike components, with the amplitude of the aberrations subject to upper bounds. This type of aberrations was first generated with a set of initial Zernike coefficients c_m based on Equations (3-5), and then rescaled to a maximum RMS of Ω wavefront distortion (e.g., $\Omega = 1, 2, \text{or } 4$ rad) to obtain the final Zernike coefficients $c_{m-final}$:

$$c_{m-final} = \frac{\Omega}{RMS_T} c_m, \quad for\ m \le M. \quad (8)$$

These aberrated training data were used to train the general DeAbe models (i.e., all but the model trained to counter the defocus mode specifically) used in all figures and videos showing simulated phantoms.

2) a single aberration mode of defocus with amplitude subject to upper bounds, i.e., the upper bounds of each Zernike coefficient were zeros except for the defocus mode (m =4):

$$T_m = \begin{cases} 1.5, & for\ m = 4 \\ 0, & otherwise\ for\ m \le M. \end{cases} \quad (9)$$

By replacing Equation (4) with Equation (9), we could generate the defocus aberration the same way as for the first aberration type (1). These training data were only used to train the specific defocus DeAbe model used in **Supplementary Fig 4**.

For each training session, we created 50 phantoms, each consisting of different random objects. For each phantom, we generated 10 independent aberrated images with each image containing random mixtures of aberrations (**Fig 1, Supplementary Figs 1-5, Supplementary Videos 1-2**) or only defocus aberrations (**Supplementary Fig 4**), for a total of 500 training data pairs per session. We also added Poisson noise to the aberrated images by defining the SNR as

$$SNR = \sqrt{S}, \quad (10)$$

where *S* is the signal defined by the average of all pixels with intensity above a threshold (here set as 1% of the maximum intensity of the blurred objects in the noise-free image).

We employed 3D RCAN to train the DeAbe model based on simulated training data. We set the number of epochs to 200; the number of steps per epoch to 400; the training patch size to 64 × 64 × 64; the number of residual blocks to 5; the number of residual groups to 5; and the number of channels to 32. Training was performed with Python 3.7.0 on a Windows 10 workstation (CPU: Intel Xeon, Platinum 8369B, two processors; RAM: 256 GB; GPU: NVIDIA GeForce RTX 3090 with 24 GB memory).

To benchmark the performance of the DeAbe model, we created synthetic phantoms with three types of aberrations:

1) a random mixture of aberrations containing different Zernike components, with the amplitude of the aberrations subject to upper bounds. This type of aberration is the same used for training the general DeAbe models and was generated following Equations (3-5) and (8). This aberration mixture was used in **Fig 1, Supplementary Fig 2, and Supplementary Videos 1-2**.

`

2) a random mixture of aberrations containing different Zernike components, with the amplitude of the aberrations fixed at a certain RMS value. This aberration mixture was first generated with a set of initial Zernike coefficients c_z based on Equations (3-5), and then rescaled to a fixed amplitude with RMS Υ (e.g., $\Upsilon = 1,2, \text{or } 4$ rad) wavefront distortion to obtain the final Zernike coefficients $c_{m-final}$:

$$c_{m-final} = \frac{\Upsilon}{RMS_c} c_m, \quad for\ m \leq M. \tag{11}$$

This aberration mixture was used for **Supplementary Figs 1,3,5**.

3) single aberration modes with a fixed RMS value, i.e., Zernike coefficients were set to zero except for the desired aberration mode. The single aberration modes tested in the paper include defocus (m=4), astigmatism (m=3,5), coma (m=7,8), trefoil (m=6,9), and spherical (m=12). If the RMS wavefront distortion is defined as Υ (e.g., $\Upsilon = 1,2, \text{or } 4$ rad), each single aberration mode's Zernike coefficients are:

Defocus: $c_4 = \Upsilon,\ otherwise\ c_m = 0\ for\ m \leq M$

Astigmatism: $\sqrt{{c_3}^2 + {c_5}^2} = \Upsilon,\ otherwise\ c_m = 0\ for\ m \leq M$

Coma: $\sqrt{{c_7}^2 + {c_8}^2} = \Upsilon,\ otherwise\ c_m = 0\ for\ m \leq M$

Trefoil: $\sqrt{{c_6}^2 + {c_9}^2} = \Upsilon,\ otherwise\ c_m = 0\ for\ m \leq M$

Spherical: $c_{12} = \Upsilon,\ otherwise\ c_m = 0\ for\ m \leq M$

These aberrations were used to test the DeAbe performance on single aberration modes (**Supplementary Figs. 3,4**).

For quantitative analysis, we used structural similarity index (SSIM) and peak signal-to-noise ratio (PSNR) to evaluate the restored images provided by deep learning as well as by traditional deconvolution. The SSIM and PSNR were calculated based on image volumes with MATLAB (Mathworks, R2022b). Their mean value and standard deviation were computed from 100 simulations, each with random object structures and input aberrations.

Preprocessing, attenuation correction, traditional deconvolution, and multiview fusion

Raw images acquired with iSIM and light sheet imaging were preprocessed by subtracting a uniform background with intensity equivalent to the average of 100 dark (no excitation light) background images. When diSPIM was operated in stage scan mode, the images were also deskewed to correct the distortion induced by stage-scan acquisition before further processing.

For the cleared mouse embryos imaged with confocal microscopy (**Fig 3, Supplementary Fig. 10, Supplementary Video 8**), raw data was additionally preprocessed with intensity attenuation correction. The attenuation correction was performed by multiplying the raw intensity values with an exponential compensation factor:

$$I(z) = I_0(z)e^{\alpha z} \tag{11}$$

with $I_0(z)$ the raw intensity, z the depth and α the attenuation factor. Here we set $\alpha = 0.01$.

For the comparison of DeAbe with traditional deconvolution, we implemented both Richardson-Lucy (RL) deconvolution[37,38] (**Fig. 1c-f, Fig. 2 and Supplementary Figs. 8-10**) and blind deconvolution[16] (**Fig. 1c-f**) on the raw aberrated images. For blind deconvolution, we used the MATLAB function *deconvblind* with default settings (https://www.mathworks.com/help/images/ref/deconvblind.html). For RL deconvolution, we adopted our previously developed deconvolution package[8] (https://github.com/eguom/regDeconProject). In one synthetic dataset ('RL Decon 2', **Fig. 1c-f**), we used

an aberrated PSF that was generated as described in **Supplementary Note 1** and matched the aberrations in the synthetic dataset; otherwise, we used an aberration-free ideal PSF for all other datasets (**Fig. 1c-f, Fig. 2 and Supplementary Figs. 8-10**). Additionally, we also performed RL deconvolution on several datasets after DeAbe processing (**Fig. 2b-d, Supplementary Fig. 8, 10**), setting the number of iterations to 20 unless specified otherwise. All deconvolution was performed in MATLAB (MathWorks, R2022b) on a Windows 10 workstation (CPU: Intel Xeon, Platinum 8369B, two processors; RAM: 256 GB; GPU: NVIDIA GeForce RTX 3090 with 24 GB memory).

For data acquired by diSPIM, we performed multiview fusion on several datasets either for generating DL training data (**Fig. 4**, **Supplementary Figs. 14, 15, 19-21, 23**) or for comparisons to the DL Decon model (**Supplementary Figs. 17, 22**). The diSPIM data typically contain two view volumes, referred to as View A and View B volumes. The multiview fusion process involves registration and joint deconvolution to combine two views into a single volumetric image stack with improved resolution. The registration first rotates View B by 90 degrees along the Y-axis to align View B's orientation with View A and then maximizes the cross-correlation function between View A and View B with affine transformations. After registration, View A and registered View B were deconvolved jointly using a modified Richardson–Lucy deconvolution algorithm as previously described[25]. Multiview fusion was achieved using custom software (https://github.com/eguom/diSPIMFusion) on a Windows 10 workstation (CPU: Intel Xeon, Platinum 8369B, two processors; RAM: 256 GB; GPU: NVIDIA GeForce RTX 3090 with 24 GB memory).

Sample preparation and imaging

Live nematode embryos imaged with light sheet microscopy

Nematode strains were kept at 20°C, and grown on NGM media plates seeded with *E. coli* OP50. Strains used in this paper included BV514 (ujIS113 [*pie-1p::mCherry::H2B + unc-119(+); Pnhr-82::mCherry::histone + unc-119(+)*]), OD58 (ltIs38 [*pie1p::GFP::PH(PLC1delta1) + unc-119(+)*]), DCR6268 (olaEx3632 [*pttx-3b::SL2::PHD::GFP:: unc-54 3' UTR + pelt-7::mCh::NLS::unc-54 3' UTR*]), and SLS164 (ltIS138[*pie-1p::GFP::PH(PLC1delta1) + unc-119(+)*]; ujIS113 [*pie-1p::mCherry::H2B + unc-119(+); Pnhr-82::mCherry::histone + unc-119(+)*]). SLS164 was made by crossing together strains BV514 and OD58 and may have unc-119(ed3) III in the background. Strains BV514 and OD58 were gifts from Dr. Zhirong Bao.

Nematode samples were prepared for diSPIM imaging as previously described[17,26,39]: gravid adult hermaphrodites were picked into a watch glass with M9 buffer, adults were cut in half to liberate embryos, and embryos were transferred onto a poly-L-lysine coated coverslip in a diSPIM imaging chamber. For strain DCR6268 ((olaEx3632 [*pttx-3b::SL2::PHD::GFP:: unc-54 3' UTR + pelt-7::mCh::NLS::unc-54 3' UTR*]), labeling neuron and gut cells), embryos were imaged once they reached the bean stage of development using a fiber-coupled symmetric diSPIM (with 0.8NA/0.8NA objectives)[26]. Volumes were captured once per minute over two hours in light sheet scan mode. Each volume comprised 50 slices, with a 1 μm step size and a total acquisition time per volume of ~1 second. For strain SLS164 (labeling cell membrane and nuclei), embryos were imaged from the 2- or 4-cell stage using a fiber-coupled asymmetric diSPIM (with 1.1NA/0.67NA objectives)[18]. Volumes were captured once every 3 minutes over 450-minute duration in stage scan mode. Each volume comprised 70 slices, with a 1.1 μm stage step size and a total acquisition time of ~1.4 s per volume. For strain BV514 (labeling cell nuclei), embryos were imaged from the bean stage to hatching using the asymmetric diSPIM. Volumes were captured every 5 minutes in stage scan mode. Each volume comprised 60 slices, with a 1.4 μm stage step size and a total acquisition time per volume of ~1.2 seconds. For strain OD58 (labeling

`

cell membranes), embryos were imaged from the 4- or 8-cell stage using a symmetric diSPIM. Volumes were captured once every 3 minutes over a 450-minute period in light sheet scan mode. Each volume comprised 45 slices, with a 1 μm step size and a total acquisition time per volume of ~0.9 seconds. For all imaging, images were acquired using 488 nm excitation (for GFP labels) or 561 nm excitation (for mCherry labels).

Expanded nematode embryos

C. elegans embryos from strain DCR6268 (labeling neurites and gut cells) were immobilized on Poly-L-Lysine (PLL) coated glass bottom dishes, bleached, digested by yatalase, fixed, and expanded. The procedure takes approximately 2 days, and is adapted from our published method[22].

First, glass bottom dishes were coated with PLL. PLL (Sigma, Cat# P5899) powder was reconstituted in distilled water to 1mg/mL, aliquoted, and stored at -20°C. Prior to experiments, 30-50 μL of PLL was placed on the glass bottom dish (MatTek, Cat# P35G-1.5-14-C) and air dried at room temperature (RT). Coated coverslips were usually prepared up to 1 day before pre-treatment of *C. elegans* for expansion microscopy.

Second, embryos were digested, fixed, and stained with DAPI. Gravid adult *C. elegans* worms were deposited in a petri dish in PBS buffer and cut with a surgical blade to release eggs. Eggs were immobilized on a PLL coated glass bottom dish in PBS and could be processed immediately or stored at 25°C in M9 buffer until the embryos developed to the desired stage. Embryos were treated with a bleaching mixture containing 1% sodium hypochlorite (Sigma, Cat# 425044) in 0.1M NaOH/water for 2-3 minutes, rinsed 3 times in PBS, digested in 50 mg/mL Yatalase in PBS (Takara Bio, Cat# T017) for 40 minutes at RT and rinsed 3 times with PBS. It was important to treat eggs with bleach only after immobilization on the PLL surface, otherwise embryos tended to detach from the glass at later steps. Digested embryos were fixed in 4% paraformaldehyde/PBS (Electron Microscopy Sciences, Cat# RT15710) for 1 hour, then rinsed 3 times with PBS to remove fixative. Fixed embryos were permeabilized in 0.1% Triton X-100/PBS (Sigma, Cat# 93443) for 1 hour at RT with 1 μL/mL of DAPI (Thermo Fisher Scientific, Cat# D1306).

Optionally, GFP signal can be boosted by immunolabeling. Yatalase digested embryos were permeabilized with staining buffer (0.1% Triton X-100/PBS) for 1 hour before immunolabeling. Embryos were stained by an anti-GFP primary antibody (Abcam, Cat# ab290) in the staining buffer at 4°C overnight at 1 μg/mL. After primary antibody labeling, embryos were washed 3 times (30 min intervals between washes) in the staining buffer and labeled using donkey-anti-rabbit-biotin secondary antibody (Jackson ImmunoResearch, Cat# 711-067-003) in the staining buffer at 4°C overnight at 1 μg/mL. After secondary antibody labeling, the embryos were washed 3 times in the staining buffer (30 mins intervals between washes) and labeled with Alexa Fluor 488 Streptavidin in the staining buffer at 4°C overnight at 2 μg/mL (Jackson ImmunoResearch, Cat# 016-540-084). Labeled embryos were washed 3 times in the staining buffer (30 minutes between washes) before being processed for expansion microscopy. Immunolabeling was only performed on the data shown in **Supplementary Fig 18a**.

Finally, embryos were expanded. Embryos were treated with 1 mM MA-NHS (Sigma, Cat# 730300) in PBS for 1 hour at RT. Samples were rinsed 3 times in PBS, and treated with monomer solution, which was made up of acrylamide (Sigma, Cat# A9099), sodium acrylate (Santa Cruz Biotechnology, Cat# 7446-81-3), N, N'-methylenebis(acrylamide) (Sigma, Cat# 146072) and 4-Hydroxy-TEMPO (Sigma, Cat# 176141), diluted with PBS, with a final concentration of 10%, 19%, 0.1%, and 0.01%, respectively. After the treatment for 1 hour at RT, the monomer solution was replaced by gelation

`

solution. The gelation solution shared the same reagents and concentrations as monomer solution, with the addition of tetramethylethylenediamine (TEMED, Thermo Fisher Scientific, Cat# 17919, reaching a final concentration of 0.2%) and ammonium persulfate (APS, Thermo Fisher Scientific, Cat# 17874, reaching a final concentration of 0.2%). APS was added at last, and the fresh gelation solution was immediately applied to the embryos sandwiched between the glass bottom dish and another coverslip surface for 2 hours at RT. It was important to control the gelation speed with 4-hydroxy-TEMPO as premature gelation can distort embryos and result in poor expansion quality. The polymerized embryo-hydrogel hybrid was cut out by a razor blade and digested with 0.2 mg/mL Proteinase K (Thermo Fisher Scientific, Cat# AM2548) in digestion buffer (0.5 M sodium chloride (Quality Biological, Cat # 351-036-101); 0.8 M guanidine hydrochloride (Sigma, Cat# G9284); and 0.5% Triton X-100) at 45°C overnight. Digested embryos were expanded ~3.3-3.7 fold in distilled water, exchanging the water every 30 min until expansion was complete. Expanded samples were flipped over so that embryos were 'on top' (suitable for diSPIM imaging), mounted on PLL coated #1.5 coverslips (VWR, Cat# 48393-241) and secured in an imaging chamber filled with distilled water. Finally, samples were imaged using the symmetric 0.8/0.8 NA diSPIM in stage scan mode. Depending on the orientation of embryos, ~200-300 planes were acquired for each embryo, with 1.414 μm stage step size and 20 ms per-plane exposure time.

Live nematode adults imaged with spinning disk confocal microscopy

C. elegans strain OH15500 (*otIs669[NeuroPAL]; otIs672[panneuronal::GCaMP6s]*) were raised at 20°C and grown on NGM media plates seeded with OP50 *E. coli* . Young adult worms (with 2 or less visible eggs in their uterus) were picked and immobilized inside a microfluidic chip as previously described[19]. Worms were imaged by a spinning disk confocal microscope (Nikon, Ti-e) equipped with a 60×/1.2 NA water objective (Nikon, CFI Plan Apochromat VC 60XC WI), a confocal scan unit (Yokagawa, CSU-X1) and an electron multiplying CCD (EM-CCD, Andor, iXon Ultra 897). Four excitation lasers (405 nm, 488 nm, 561 nm, and 640 nm) were used for illumination, in conjunction with emission filters spanning 420-470 nm, 500-545 nm, 570-650 nm, and 660-800 nm bandwidths, respectively. The pixel size was 0.27 μm in the XY dimension and each Z-stack volume comprised 21 slices for each color, with 1.5 μm step size. Each multicolor Z-stack volume was captured at a rate of just over 1 minute.

Fixed WGA-labeled NK-92 samples

NK-92 cells (ATCC®, CRL-2407™) were rinsed with 1× PBS, and fixed with 1 ml of 4% paraformaldehyde in 1× PBS for 30 min at room temperature, rinsed in 1 ml of 1x PBS, and permeabilized in 0.1% Triton X-100 in 1× PBS for 15 min. Next, samples were rinsed with 1× PBS, and blocked with buffer containing 1% BSA (Fisher, Cat# BP9700100) in 1× PBS for 1 hour. Blocking buffer was removed, and the samples were stained with 500 μl of 1x PBS with a 1:100 dilution of Alexa Fluor 555 labelled WGA (Invitrogen, Cat# W32464), 10 U/mL phalloidin-ATTO 647N conjugate (Millipore-Sigma, Cat #65906), and 1:1000 dilution of Hoechst solution (Tocris, Cat#5117) for 1 h. Cells were washed in 1× PBS three times. We mounted samples using 90% Glycerol (Sigma, Cat# G5516) in 1x PBS.

In preparation for imaging, cells were cultured in collagen-I gels in the ImmunoCult-XF T Cell Expansion Medium (STEMCELL Technologies, Cat# 10981) with the addition of Human Recombinant Interleukin 2 (STEMCELL Technologies, Cat# 78036.3). To prepare 3 mg/ml collagen-I gel, we assembled a gel premix on ice in a prechilled Eppendorf tube. Briefly, to 1 volume of CellAdhere™ type I bovine (STEMCELL Technologies, Cat# 07001) we added 8/10 volume of DMEM, 1/10 volume of 10x PBS, 1/20

`

volume of 1M HEPES, and 1/20 volume of 1M (in DMSO) Alexa Fluor 488 ester (Molecular Probes, Cat# A20000). A drop of premixed gel (~50 µL) was spread immediately on a glass surface of a plasma-treated glass-bottom 35 mm Petri dish (MatTek Corp., Cat# P35G-1.5-14-C) with a pipette tip. During polymerization (room temperature, for overnight), gels were covered with 1 mL of mineral oil (Sigma-Aldrich, Cat# M8410) to prevent evaporation of water. Before adding NK-92 cells, polymerized gels were rinsed with PBS to remove the unpolymerized gel components.

Instant structured illumination microscopy (iSIM) was performed using the commercial instant structured illumination microscope system (VisiTech Intl, Sunderland, UK) equipped with an Olympus UPlanSAapo 60×/1.3NA Sil objective, two Flash-4 scientific CMOS cameras (Hamamatsu, Corp., Tokyo, Japan), an iSIM scan head (VisiTech Intl, Sunderland, UK), and a Nano-Drive piezo Z stage (Mad City Laboratories, Madison, WI). The iSIM scan head included the VT-Ingwaz optical destriping unit. The exposure time was set to 250 ms per image frame. The voxel size was 64 x 64 x 250 nm, in x, y, and z, respectively.

Two-photon microscopy on live and fixed mouse tissue

Fixed mouse liver samples and fresh ex-vivo mouse heart muscle strips were imaged with two-photon microscopy using a Leica SP8 two photon DIVE upright microscope (Mannheim, Germany), a pulsed dual beam Insight X3 Ti-Sapphire laser (MKS Spectra-Physics, Milpitas CA), a Leica 25x 1.0 NA (HC PL IRAPO) water dipping lens, and emission bandwidth tunable Leica HyD detectors in the non-descanned emission pathway. Liver samples were prepared from freshly excised liver from a 10 week-old mouse expressing a membrane-targeted peptide fused with tdTomato[40]. After excision, the mouse liver was washed in cold saline three times, fixed with 4% formaldehyde in PBS for 2 hours, and stored in PBS. Tissue harvesting procedures were approved by the NCI (for mouse liver) and NHLBI (for mouse heart) Animal Care User Committees (ACUC) respectively. Freshly excised heart muscle strips from transgenic mice expressing mitochondrial TOMM20-mNeonGreen were prepared for imaging as described[41]. tdTomato and mNeonGreen were excited using 1045 nm and 960 nm excitation with emission bandwidths of 550-700 nm and 500-600 nm, respectively. Laser excitation (ramped as a function of depth in some experiments and optimized by adjusting the objective motorized correction collar) were in the range of 1% for tdTomato and less than 20% for mNeonGreen. HyD detector gains were kept at 100% for tdTomato and 150% for mNeonGreen. Tiled images volumes of liver membrane expressing tdTomato were collected with voxels sizes set to 400 nm in the XY dimension and 500 nm in the z dimension. Z-stack volumes of mNeonGreen expressing heart strip were collected with voxels sizes set to 120 nm in the XY dimension and 500 nm in the z dimension. All imaging was conducted at an imaging speed of 600 Hz with a pinhole size of 1 A.U.

Cleared mouse embryos imaged with confocal microscopy

E11.5-day mouse embryos were collected in phosphate-buffered saline (PBS) and directly immersed in 4% paraformaldehyde (PFA) in PBS (pH 7.4) at 4°C overnight. Following fixation, the samples were washed with PBS and stored in PBS at 4°C for further analyses. Wholemount immunofluorescence staining was performed at 4°C. The mouse embryos were permeabilized with 0.2% Triton/PBS overnight and blocked with 10% normal goat serum and 1% BSA in 0.2% Triton/PBS overnight. The embryos were then stained with monoclonal antibody against PECAM1 (CD31, clone MEC 13.3, Cat# 553700, BD Pharmingen, 1:200 dilution) and monoclonal anti-β-tubulin III (TuJ1)) antibody (clone 2G10, Cat# T8578, Sigma-Aldrich, 1:500 dilution) in blocking buffer overnight. After washing with 0.2% Triton/PBS, the embryos were stained with secondary antibodies with Alexa 488 goat

anti-rat IgG and Alexa 594 goat-anti-mouse IgG (1:250, Invitrogen, Carlsbad, CA) in blocking buffer overnight. The embryos were cleared with CLARITY and imaged using a Zeiss LSM 880 Confocal microscope with a 10X, 0.5NA air objective. To compensate for focal shift effects due to the refractive index difference between air and CLARITY we scaled the axial voxel size of images by 1.45 before processing for DeAbe.

Calculation of vessel orientation and alignment

Orientations were estimated in 3D using a weighted vector summation algorithm[23], adapting it for the volumetric images of fiber-like structures corresponding to the CD31 channel (i.e., blood vessel images) in CLARITY-cleared mouse embryos (**Fig. 3**).

For a given voxel within the 3D image, an $n \times n \times n$ voxel window was generated surrounding the voxel under assessment. To segment the effective voxels, six-level Otsu intensity thresholding was applied to the image, with five thresholds dividing the intensity into six levels. The lowest level was designated as background noise, and regions assigned to the upper five levels defined the vessel signals. The window size n was typically set as two to three times the vessel thickness. All vectors passing through the center voxel were defined and weighted by their length and intensity variations, and the direction of the sum of all the weighted vectors was designated as the orientation of the center voxel[23], with associated azimuthal angle θ (ranging from 0° to 180°) and polar angle φ (ranging from 0° to 180°). However, since the calculation of the polar angle φ was not straightforward, we defined two additional azimuthal angles, β and γ (**Supplementary Fig. 11a**), which were symmetrical to the azimuthal angle θ. β was defined as the angle between the projection of the vessel in the zx plane and the x axis, and γ was the angle between the projection in the yz plane and the $-y$ axis. These two angles were related to the polar angle φ via: $\tan^2\varphi = 1/\tan^2\beta + 1/\tan^2\gamma$.

We also derived the 3D directional variance (DV) metric, quantifying the spread in orientations[24,42]. The value of DV ranges from 0 to 1, with 0 corresponding to perfectly parallel alignment, and 1 corresponding to complete disorder (**Supplementary Fig. 11b**). The directional variance $\bar{D}_{3D}$ was defined as:

$$\bar{D}_{3D} = 1 - (\bar{C}_{3D}{}^2 + \bar{S}_{3D}{}^2 + \bar{Z}_{3D}{}^2)^{1/2},$$

where:

$$\bar{C}_{3D} = (1/k)\sum_{j=1}^{k}(f_j/\sqrt{1+f_j^2})\cos(2\theta_j),$$

$$\bar{S}_{3D} = (1/k)\sum_{j=1}^{k}(f_j/\sqrt{1+f_j^2})\sin(2\theta_j),$$

$$\bar{Z}_{3D} = (1/k)\sum_{j=1}^{k}(SI/\sqrt{1+f_j^2}),$$

with $f_j = \sqrt{1/\tan^2(2\beta_j) + 1/\tan^2(2\gamma_j)}$, and $SI = (-1)\cdot(\varphi - 90)/|\varphi - 90|$, where φ was acquired from the determination of β and γ as described above, k was the number of fiber voxels in the region, and θ, β and γ were calculated azimuthal angles as described above.

`

Membrane segmentation

For the images of live worm embryos dual-labeled with nuclear and membrane markers (**Fig. 4c, d, Supplementary Fig. 16**), raw data was restored using our multiple-step deep learning pipeline (Steps 1-3 in **Supplementary Fig. 13a**) prior to cell membrane segmentation. We performed automatic membrane segmentation using segmented nuclei as seeds:

First we used the Keras and Tensorflow-based implementations of Mask RCNN[43] (https://github.com/matterport/Mask_RCNN) to perform nuclear segmentation (**Supplementary Fig. 16d**). We then manually segmented 8 volumes (3 acquired with diSPIM, 3 with iSPIM, and 2 from multiview confocal microscopy[22] for a total of 1963 nuclei) for training. Of these 8 volumes, 6 volumes with a total of 1688 nuclei were used for training a segmentation network and 2 volumes with a total of 275 nuclei were used for validation. We used a ResNet-50 model as the backbone for our network, initialized the model using weights obtained from pretraining on the MS COCO dataset[44], and proceeded to train all layers in three stages. Training took ~10 hours and applying the model took ~ 3 minutes per volume on a Windows workstation equipped with an Intel(R) Xeon(R) W-2145 CPU operating at 3.70 GHz, an Nvidia Quadro P6000 GPU, and 128 GB of RAM. After Mask RCNN segmentation, we applied a marker-controlled watershed operation (https://www.mathworks.com/help/images/marker-controlled-watershed-segmentation.html) to the nuclear segmentations to separate touching nuclei.

Second, we applied the vascular structure enhancement filter[45] (https://github.com/timjerman/JermanEnhancementFilter) to the membrane data to enhance boundaries (**Supplementary Fig. 16c**). Scales were set to [2.0, 2.25, 2.5] and all other parameters were set to the default.

Third, the centroids of segmented nuclei were used as seeds, and we used the seeded watershed algorithm (https://github.com/danielsnider/Simple-Matlab-Watershed-Cell-Segmentation) for membrane segmentation (**Supplementary Fig. 16f**).

This workflow was applied both to the raw image data and restored images after each step in our multi-step pipeline to demonstrate the benefit of segmentation enhancement from DL processing.

For selected volumes (**Fig. 4c, Supplementary Video 11**), we also performed manual editing on the automatic segmentations produced by the multi-step deep learning pipeline. Manual editing was performed within the ImageJ plugin Labkit (https://imagej.net/plugins/labkit/). After automatic segmentations were imported to Labkit, segmentation labels were manually edited interactively in lateral views (XY planes), and then were edited in axial views (YZ planes). Since the manual editing was conducted in 2D views and initial editing in either view was not sufficient to ensure smoothness in 3D, we iterated twice to further improve our results.

Code availability

Training and applying deep learning models were achieved using Python 3.7.0. Generation of synthetic aberrated data and quantitative image analysis was performed in MATLAB (Mathworks, R2022b). Customized code and software are available at https://github.com/eguomin/DeAbePlus/. RCAN and CARE software were installed from https://github.com/AiviaCommunity/3D-RCAN and https://github.com/CSBDeep/CSBDeep, and code for RL deconvolution and multiview fusion is available at https://github.com/eguomin/diSPIMFusion/.

Data availability

`

The data that support the findings of this study are included in **Supplementary Figs. 1–23** and **Supplementary Videos 1–14**. Some representative data from the figures (**Supplementary Figs. 6, 17**) are publicly available at https://zenodo.org/record/8424246. Other datasets (training data and intermediate data for deep learning) are available from the corresponding author upon reasonable request due to their large file size.

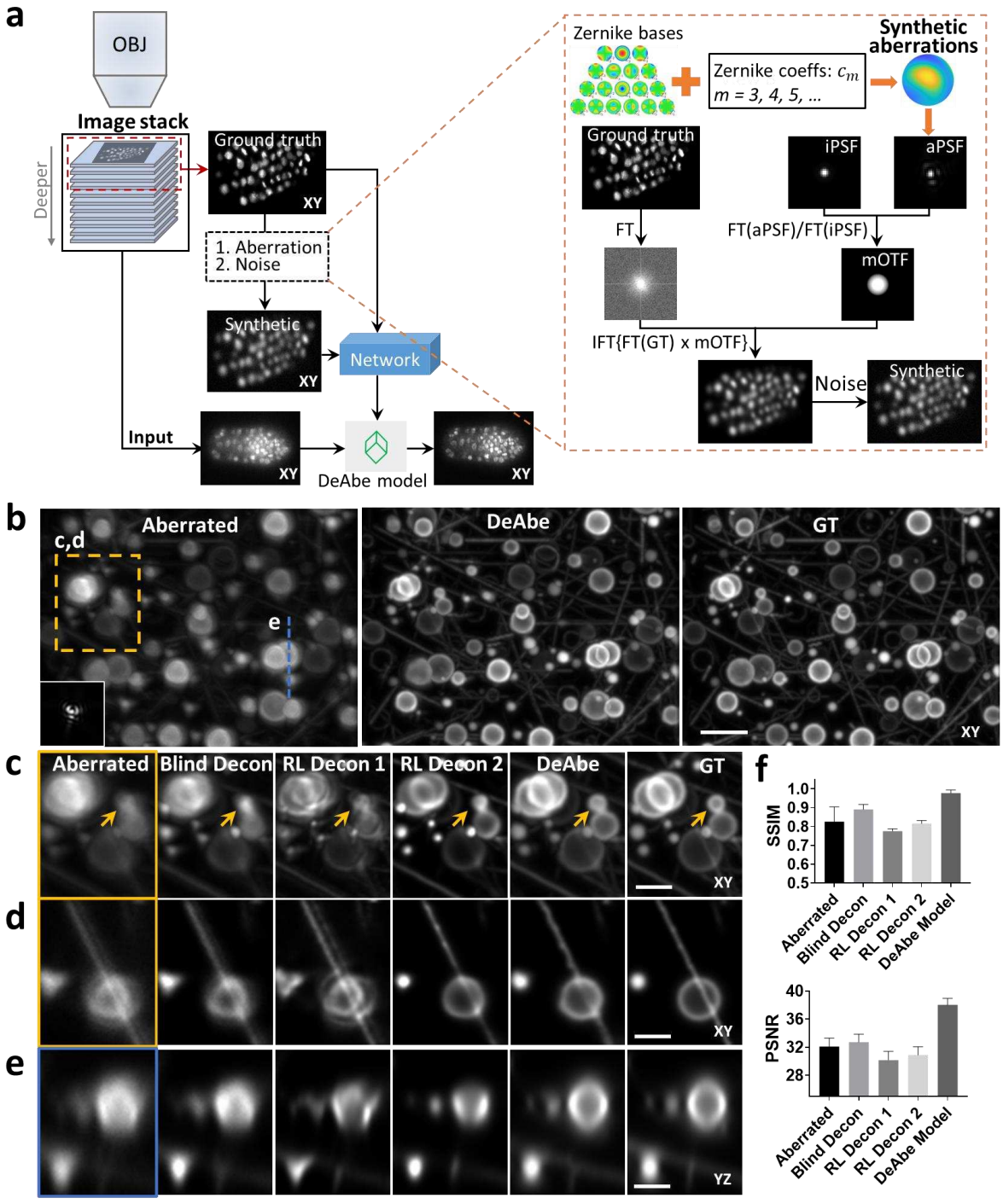

Fig. 1, Concept and simulations illustrating deep learning-based aberration compensation. a) Schematic. *Left*: Fluorescence microscopy volumes are collected and near-diffraction-limited images from the shallow side of each stack are synthetically degraded to resemble aberrated images deeper into the stack. A neural network (e.g., a three-dimensional residual channel attention network, 3D RCAN) is trained to reverse this degradation given the ground truth on the shallow side of the stack, and the trained neural network (DeAbe model) subsequently applied to images throughout the stack,

`

improving contrast and resolution. *Right*: More detailed view of synthetic degradation process. Zernike basis functions and associated coefficients (coeffs) are used to add random aberrations by modifying the ideal point spread function (iPSF) to generate an aberrated PSF (aPSF). Ground truth images (GT) are Fourier transformed (FT) and multiplied by the ratio of the Fourier transformed aberrated and ideal PSFs (essentially a modified optical transfer function, mOTF). Inverse Fourier transforming (IFT) the result and adding noise generates the synthetically aberrated images. See **Methods** for further detail on this procedure. OBJ: objective lens used to collect the stack. **b)** Simulated three-dimensional phantoms consisting of randomly oriented and positioned dots, lines, spheres, spherical shells, and circles comparing maximum intensity projections of aberrated input image (left, random aberration with root mean square (RMS) wavefront distortion < 2 radians and Poisson noise added for an SNR of ~16, corresponding PSF in inset), network prediction (DeAbe) given aberrated input (middle), and ground truth (GT, right). Higher magnification views of dashed rectangular region are shown in **c)** (maximum intensity projection) and **d)** (single plane), additionally showing restoration given blind deconvolution (Blind Decon), Richardson-Lucy deconvolution with diffraction-limited PSF (RL Decon 1), Richardson-Lucy deconvolution with aberrated PSF (RL Decon 2). Yellow arrows indicate a reference structure for visual comparison. Twenty iterations were used for RL deconvolution and ten for blind deconvolution. **e)** As in **c, d**) but showing axial plane along dashed blue line in **b)**. **f)** Quantitative comparisons for the restorations shown in **b-e**) using structural similarity index (SSIM, top) and peak signal-to-noise ratio (PSNR, bottom) with ground truth reference. Means and standard deviations are shown for 100 simulations (10 independent phantom volumes, each aberrated with 10 randomly chosen aberrations). Scale bars: 5 μm **b)** and 2.5 μm **c-e)**. See also **Supplementary Figs. 1-5**.

`

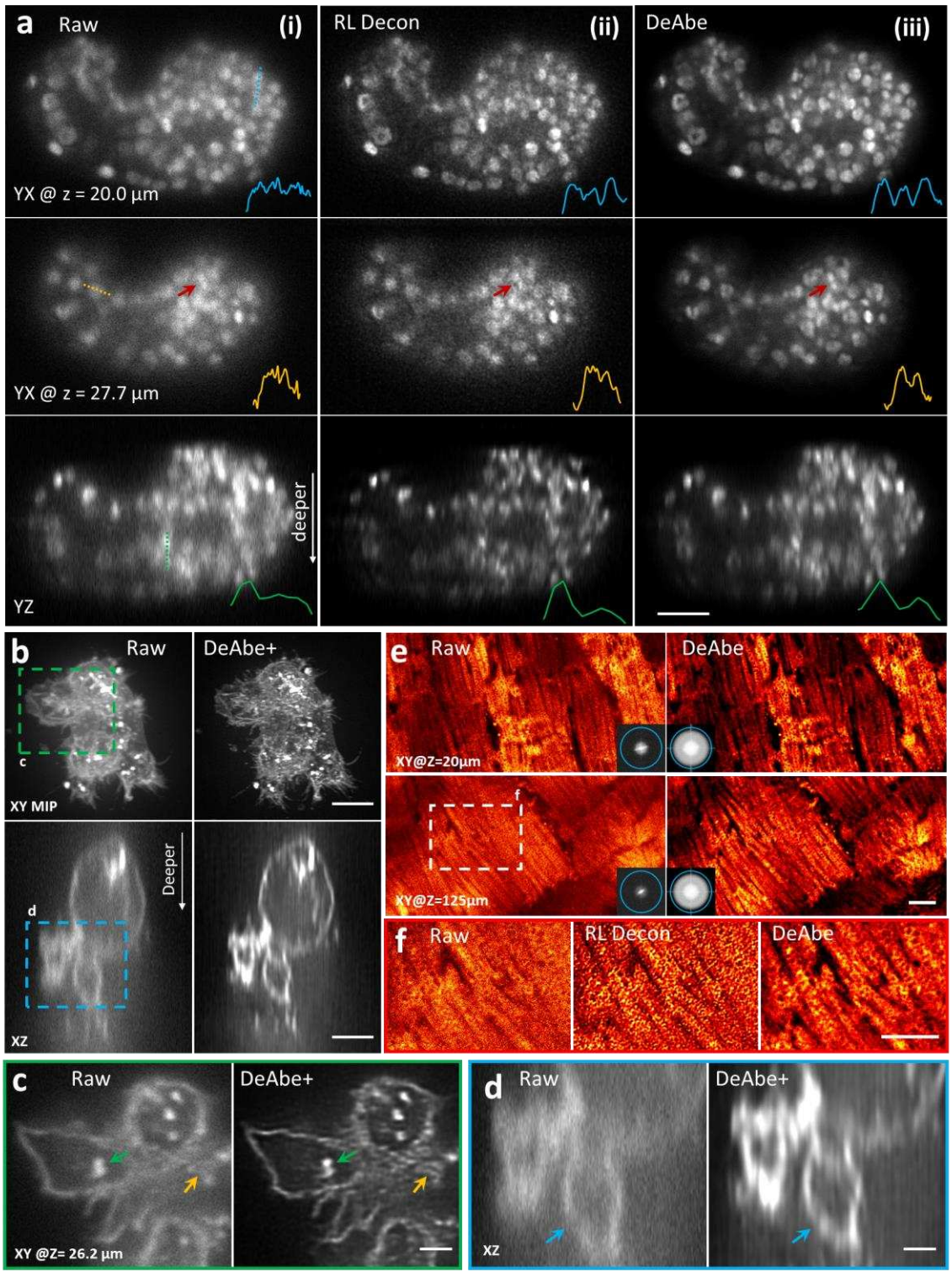

788

789 **Figure 2, Computational aberration compensation on fluorescence microscopy image volumes. a)** Live
790 *C. elegans* embryos expressing a pan-nuclear GFP histone marker were imaged with light sheet
791 microscopy (**i**, left column) and the raw data processed with Richardson-Lucy deconvolution (**ii**, 10
792 iterations, middle column) or with a trained DeAbe model (**iii**, right column). First two rows show single

`

planes 20 and 28 μm into the sample, third row shows axial view. Comparative line profiles through dashed blue, yellow, and green lines are shown in insets, comparing ability to discriminate nuclei. Red arrow highlights nuclei for visual comparison. See also **Supplementary Video 3**. **b)** NK-92 cells stained with Alexa Fluor 555 wheat germ agglutinin and embedded in collagen matrices were fixed and imaged with instant SIM, a super-resolution imaging technique. Left: raw data, right: after application of DeAbe and deconvolution (DeAbe+, 20 iterations Richardson-Lucy). Lateral maximum intensity projections (MIP, top) or single axial planes (bottom) are shown in **b)**, and **c, d** show higher magnification views corresponding to green **c)** or blue **d)** dashed rectangular regions in **b)**. Colored arrows in **c, d** highlight fine features obscured in the raw data and better revealed in the DeAbe+ reconstructions. See also **Supplementary Video 5**, **Supplementary Fig. 8. e)** Live cardiac tissue containing cardiomyocytes expressing Tomm20-GFP was imaged with two photon microscopy. Raw data (left) are compared with DeAbe prediction (right) at indicated depths, with insets showing corresponding Fourier transform magnitudes. Blue circles in Fourier insets in **e)** indicate 1/300 nm^{-1} spatial frequency just beyond resolution limit. See also **Supplementary Video 6**. **f)** Higher magnification views of white dashed rectangular region in **e)**, emphasizing recovery of mitochondrial boundaries by DeAbe model. See also **Supplementary Fig. 9, Supplementary Video 7.** Scale bars: 10 μm **a, e)**; 5 μm **b, f)**; 2 μm **c, d)**; **e**) diameter of Fourier circle: 300 nm^{-1}.

`

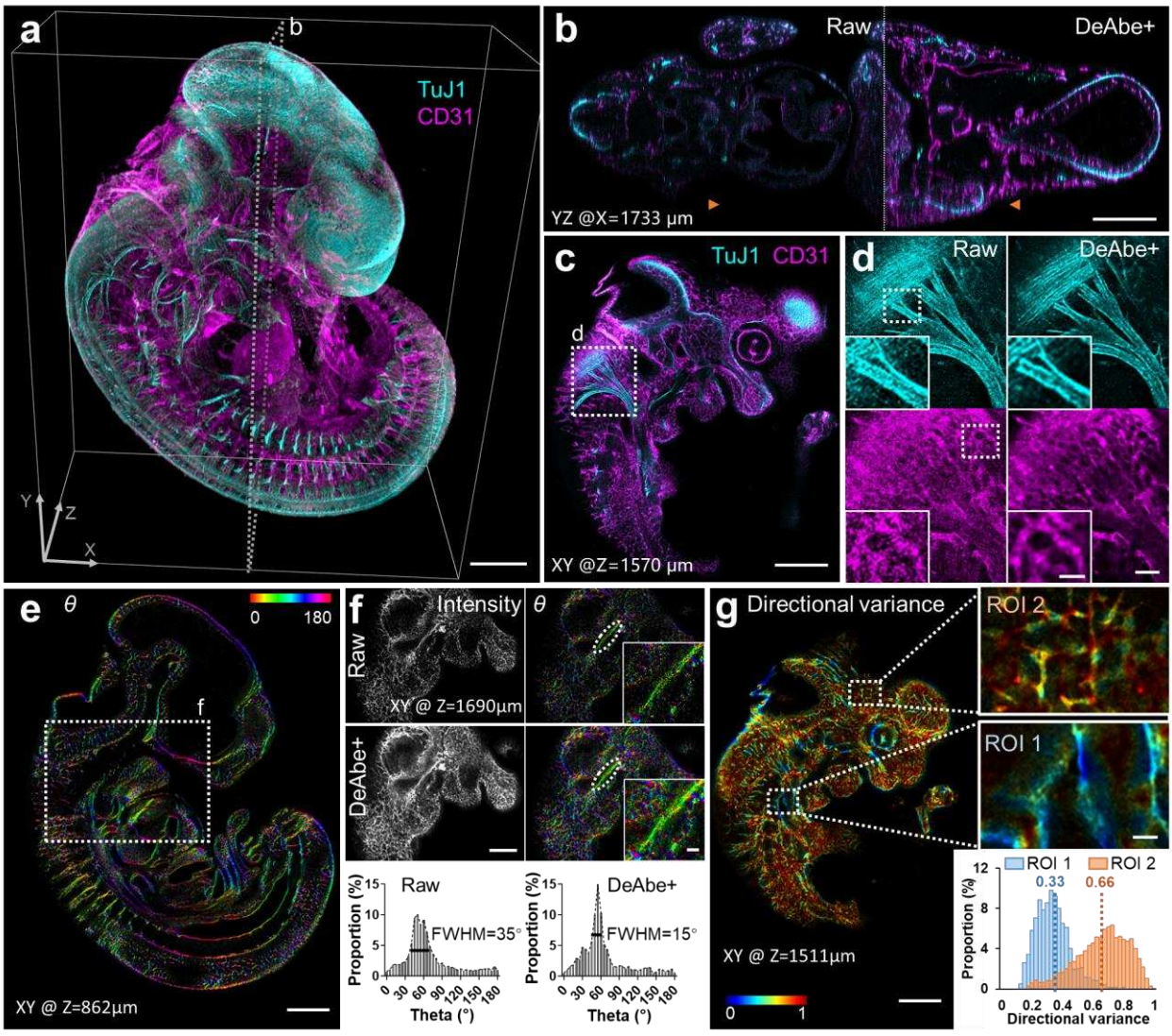

Fig. 3, Computational aberration compensation on mm-scale cleared mouse embryo volumes. a) Fixed and CLARITY-cleared E11.5-day mouse embryos were immunostained for neurons (TuJ1, cyan) and blood vessels (CD31, magenta), imaged with confocal microscopy and processed with a trained DeAbe model. See also **Supplementary Video 8**. **b)** Axial view corresponding to dotted rectangular region in **a)**, comparing raw data and depth-compensated, de-aberrated, and deconvolved data (DeAbe+). See also **Supplementary Fig. 10**. **c)** Higher magnification lateral view at axial depth of 1570 µm indicated by the orange double headed arrowheads in **b)**. **d)** Higher magnification views of white dotted region in **c)**, comparing raw (left) and DeAbe+ processing (right) for neuronal (top) and blood vessel (bottom) stains. **e)** Orientation (θ, transverse angle) analysis on blood vessel channel of DeAbe+ data, here shown on single lateral plane at indicated axial depth. See also **Supplementary Fig. 11, Supplementary Video 9**. **f)** Higher magnification lateral view of white dotted region in **e)** (note that axial plane is different), comparing intensity (left) and orientation (right) views between raw (top row) and DeAbe+ prediction

`

(middle row). Righthand insets show higher magnification views of vessel and surrounding region highlighted by dotted lines. Bottom row indicates histogram of all orientations in the vessel highlighted with dotted ellipse, full-width-at-half maximum (FWHM) in peak region of histogram is also shown. **g)** Directional variance of blood vessel stain within the indicated plane, with higher magnification region of interest (ROI) views at right. Histogram of directional variance in both regions also shown. See also **Supplementary Fig. 12**. Scale bars: 500 μm **a, b, c, e)**; 100 μm **d)**, 50 μm inset; 300 μm **f)**, 50 μm inset; 300 μm **g)**, 50 μm inset.

`

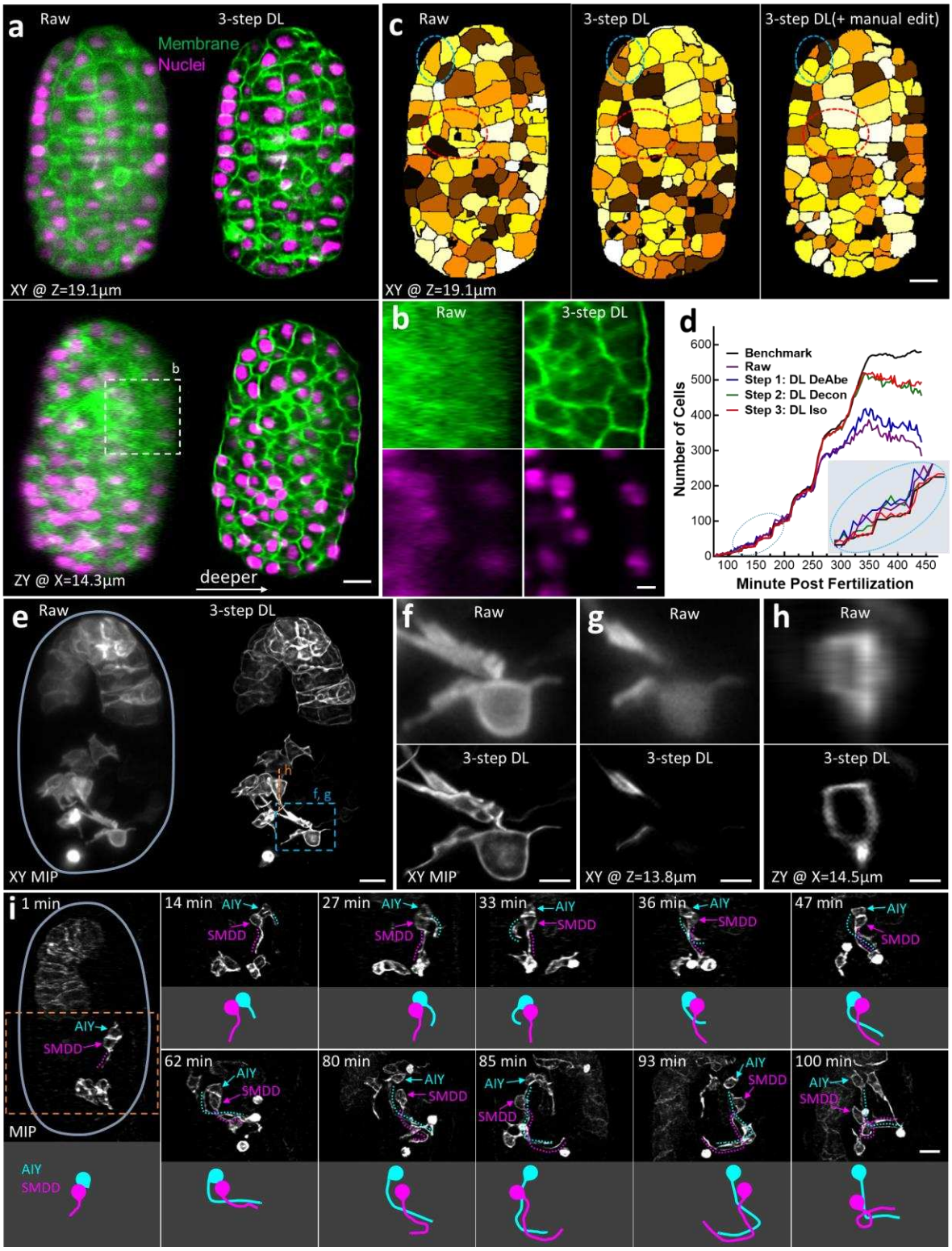

837

838 **Fig. 4, Incorporating aberration compensation into multi-step restoration dramatically improves**
839 **image quality in volumetric time-lapse imaging. a)** *C. elegans* embryos expressing GFP-labeled
840 membrane marker (green) and mCherry-labeled nuclear marker (magenta) were imaged with dual-view

`

light-sheet microscopy (diSPIM) and the raw data (left) from single-view recordings processed through neural networks that progressively de-aberrated, deconvolved, and isotropized spatial resolution (3-step DL, right). Single planes from lateral (top) and axial (bottom) perspectives are shown, with arrow in lower panel indicating direction of increasing depth. See also **Supplementary Video 10**, **Supplementary Figs. 14, 15**. **b)** Higher magnification axial views of membranes (top) and nuclei (bottom) deep into embryo, corresponding to dashed rectangle in **a)**. **c)** Examples of automatic segmentation on raw (left, 319 cells), 3-step DL prediction (middle, 421 cells), and manually corrected segmentation based on DL prediction (right, 421 cells). Single planes corresponding to the upper planes in **a)** are shown. Red and blue dashed ellipses highlight regions for visual comparison. See also **Supplementary Video 11**. **d)** Number of cells detected by automatic segmentation of membrane marker vs. time for raw data (purple), and after successively applying each step in the multistep restoration (Steps 1-3, blue, green, and red curves). Ground truth from manual expert (black curve) is also shown for comparison. Inset (ellipse with dotted blue lines) highlights number count at early timepoints. **e)** Maximum intensity projection (MIP) images of *C. elegans* embryos expressing membrane-localized GFP under control of the *ttx3-3b* promoter, imaged with diSPIM, comparing raw single-view recordings (left) and multi-step restoration that progressively de-aberrated, deconvolved, and super-resolved the data (right, 3-step DL). Boundary of the embryo has been outlined in light blue for clarity. See also **Supplementary Figs. 19, 20, Supplementary Video 12.** Higher magnification MIP (**f**) or single lateral (**g**) or axial (**h**) plane comparisons corresponding to dashed lines or rectangle in **e**) are also shown. **i)** Time series based on 3-step DL MIP predictions highlight developmental progression of AIY (blue) and SMDD (magenta) neurites as they enter the nerve ring region. Top and bottom parts of each panel at each time point show MIP (neurites highlighted as dotted lines) vs. model of the neurites, respectively. See also **Supplementary Fig. 21**. Scale bars: 5 μm **a, c, e, f, h**); 2 μm **b, d, g**).

`

865

866 1 Ji, N. Adaptive optical fluorescence microscopy. *Nature Methods* **14**, 374 (2017).
867 2 Hampson, K. M. *et al.* Adaptive optics for high-resolution imaging. *Nat Rev Methods Primers* **1**,
868 1-26 (2021).
869 3 Wang, K. *et al.* Rapid adaptive optical recovery of optimal resolution over large volumes. *Nat*
870 *Methods* **11**, 625-628 (2014).
871 4 Zheng, W. *et al.* Adaptive optics improves multiphoton super-resolution imaging. *Nat Methods*
872 **14**, 869-872 (2017).
873 5 Weigert, M. *et al.* Content-aware image restoration: pushing the limits of fluorescence
874 microscopy. *Nat Methods* **15**, 1090-1097 (2018).
875 6 Qiao, C. *et al.* Rationalized deep learning super-resolution microscopy for sustained live imaging
876 of rapid subcellular processes. *Nat Biotechnol.* (2022). https://doi.org:doi: 10.1038/s41587-022-
877 01471-3
878 7 Li, Y. *et al.* Incorporating the image formation into deep learning improves network
879 performance. *Nature Methods* (2022). https://doi.org:doi: 10.1038/s41592-022-01652-7
880 8 Guo, M. *et al.* Rapid image deconvolution and multiview fusion for optical microscopy. *Nature*
881 *Biotechnol.* **38**, 1337-1346 (2020). https://doi.org:https://doi.org/10.1038/s41587-020-0560-x
882 9 Chen, J. *et al.* Three-dimensional residual channel attention networks denoise and sharpen
883 fluorescence microscopy image volumes. *Nature Methods* **18**, 678-687 (2021).
884 https://doi.org:https://doi.org/10.1101/2020.08.27.270439
885 10 Wang, H. *et al.* Deep learning enables cross-modality super-resolution in fluorescence
886 microscopy. *Nat Methods* **16**, 103-110 (2019).
887 11 Tian, Q. *et al.* DNN-based aberration correction in a wavefront sensorless adaptive optics
888 system. *Optics Express* **27**, 10765-10776 (2019).
889 12 Saha, D. *et al.* Practical sensorless aberration estimation for 3D microscopy with deep learning.
890 *Opt Express* **28**, 29044-29053 (2020).
891 13 Vinogradova, K. & Myers, E. W. Estimation of Optical Aberrations in 3D Microscopic Bioimages.
892 *2022 7th International Conference on Frontiers of Signal Processing (ICFSP)*, 97-103 (2022).
893 https://doi.org:doi: 10.1109/ICFSP55781.2022.9924879
894 14 Hanser, B. M., Gustafsson, M. G. L., Agard, D. A. & Sedat, J. W. Phase retrieval for high-
895 numerical-aperture optical systems. *Optics Letters* **28**, 801-803 (2003).
896 15 Hanser, B. M., Gustafsson, M. G. L., Agard, D. A. & Sedat, J. W. Phase-retrieved pupil functions in
897 wide-field fluorescence microscopy. *J Microsc.* **216(Pt 1)**, 32-48 (2004).
898 16 Holmes, T. J. *et al.* in *Handbook of Biological Confocal Microscopy* (ed James B. Pawley) 389-
899 402 (Springer, 1995).
900 17 Wu, Y. *et al.* Inverted selective plane illumination microscopy (iSPIM) enables coupled cell
901 identity lineaging and neurodevelopmental imaging in Caenorhabditis elegans. *Proc. Natl. Acad.*
902 *Sci. USA* **108**, 17708-17713 (2011).
903 18 Wu, Y. *et al.* Reflective imaging improves spatiotemporal resolution and collection efficiency in
904 light sheet microscopy. *Nat Commun.* **8**, 1452 (2017).
905 19 Yemini, E. *et al.* NeuroPAL: A Multicolor Atlas for Whole-Brain Neuronal Identification in *C.*
906 *elegans*. *Cell* **184**, 272-288 (2021).
907 20 York, A. G. *et al.* Instant super-resolution imaging in live cells and embryos via analog image
908 processing. *Nat Methods* **10**, 1122-1126 (2013).
909 21 Chung, K. *et al.* Structural and molecular interrogation of intact biological systems. *Nature* **497**,
910 332-337 (2013).

`

22 Wu, Y. *et al.* Multiview confocal super-resolution microscopy. *Nature* **600**, 279-284 (2021). https://doi.org:https://doi.org/10.1101/2021.05.21.445200

23 Liu, Z. *et al.* Rapid three-dimensional quantification of voxel-wise collagen fiber orientation. *Biomedical Optics Express* **6**, 2294-2310 (2015).

24 Liu, Z. *et al.* Automated quantification of three-dimensional organization of fiber-like structures in biological tissues. *Biomaterials* **116**, 34-47 (2017).

25 Wu, Y. *et al.* Spatially isotropic four-dimensional imaging with dual-view plane illumination microscopy. *Nat Biotechnol.* **31**, 1032-1038 (2013).

26 Kumar, A. *et al.* Dual-view plane illumination microscopy for rapid and spatially isotropic imaging. *Nature Protocols* **9**, 2555-2573 (2014).

27 Cao, J. *et al.* Establishment of a morphological atlas of the *Caenorhabditis elegans* embryo using deep-learning-based 4D segmentation. *Nature Communications* **11**, 6254 (2020).

28 Sulston, J. E., Schierenberg, E., White, J. G. & Thomson, J. N. The embryonic cell lineage of the nematode Caenorhabditis elegans. *Dev. Biol.* **100**, 64-119 (1983).

29 Chen, F., Tillberg, P. & Boyden, E. S. Expansion microscopy. *Science* **347**, 543-548 (2015).

30 Bertrand, V. & Hobert, O. Linking Asymmetric Cell Division to the Terminal Differentiation Program of Postmitotic Neurons in *C. elegans*. *Developmental Cell* **16**, 563-575 (2009).

31 Rapti, G., Li, C., Shan, A., Lu, Y. & Shaham, S. Glia initiate brain assembly through noncanonical Chimaerin-Furin axon guidance in *C. elegans*. *Nature Neuroscience* **20**, 1350-1360 (2017).

32 Moyle, M. W. *et al.* Structural and developmental principles of neuropil assembly in *C. elegans*. *Nature* **591**, 99-104 (2021).

33 Brittin, C. A. *et al.* Multicellular rosettes organize neuropil formation. *bioRxiv* (2020).

34 White, J. G., Southgate, E., Thomson, J. N. & Brenner, S. The Structure of the Nervous System of the Nematode Caenorhabditis elegans. *Phil. Trans. R. Soc. London Ser. B* **314**, 1-340 (1986).

35 Mori, I. & Ohshima, Y. Neural regulation of thermotaxis in *Caenorhabditis elegans*. *Nature* **376**, 344-348 (1995).

36 Thibos, L. N., Applegate, R. A., Schwiegerling, J. T., Webb, R. & Members, V. S. T. Standards for Reporting the Optical Aberrations of Eyes. *OSA Technical Digest*, SuC1 (2000).

37 Richardson, W. H. Bayesian-Based Iterative Method of Image Restoration. *JOSA* **62**, 55-59 (1972).

38 Lucy, L. B. An iterative technique for the rectification of observed distributions. *Astronomical Journal* **79**, 745-754 (1974).

39 Bao, Z. & Murray, J. I. in *Imaging in Developmental Biology: A Laboratory Manual* (eds James Sharpe, Rachel Wong, & Raphael Yuste) (Cold Spring Harbor Laboratory Press, 2010).

40 Muzumdar, M. D., Tasic, B., Miyamichi, K., Li, L. & Luo, L. A global double-fluorescent Cre reporter mouse. *Genesis* **45**, 593-605 (2007).

41 Kosmach, A. *et al.* Monitoring mitochondrial calcium and metabolism in the beating MCU-KO heart. *Cell Reports* **37**, 109846 (2021).

42 Liu, Z. *et al.* Label-free, multi-parametric assessments of cell metabolism and matrix remodeling within human and early-stage murine osteoarthritic articular cartilage. *Communications Biology* **6**, 405 (2023).

43 He, K., Gkioxari, G., Dollár, P. & Girshick, R. Mask R-CNN. *2017 IEEE conference on Computer Vision (ICCV)*, 2980-2988 (2017).

44 Lin, T.-Y. *et al.* in *ECCV 2014* Vol. 8693 (eds D. Fleet, T. Pajdla, B. Schiele, & T. Tuytelaars) (Springer, 2014).

45 Jerman, T., Pernuš, F., Likar, B. & Špiclin, Ž. Enhancement of Vascular Structures in 3D and 2D Angiographic Images. *IEEE Trans Med Imaging* **35**, 2107-2118 (2016).